

RESEARCH

Cosmological N-body simulations: a challenge for scalable generative models

Nathanaël Perraudin^{1*}, Ankit Srivastava¹, Aurelien Lucchi², Tomasz Kacprzak³, Thomas Hofmann² and Alexandre Réfrégier³

Abstract

Deep generative models, such as Generative Adversarial Networks (GANs) or Variational Autoencoders (VAs) have been demonstrated to produce images of high visual quality. However, the existing hardware on which these models are trained severely limits the size of the images that can be generated. The rapid growth of high dimensional data in many fields of science therefore poses a significant challenge for generative models. In cosmology, the large-scale, three-dimensional matter distribution, modeled with *N-body simulations*, plays a crucial role in understanding of evolution of structures in the universe. As these simulations are computationally very expensive, GANs have recently generated interest as a possible method to emulate these datasets, but they have been, so far, mostly limited to two dimensional data. In this work, we introduce a new benchmark for the generation of three dimensional N-body simulations, in order to stimulate new ideas in the machine learning community and move closer to the practical use of generative models in cosmology. As a first benchmark result, we propose a scalable GAN approach for training a generator of N-body three-dimensional cubes. Our technique relies on two key building blocks, (i) splitting the generation of the high-dimensional data into smaller parts, and (ii) using a multi-scale approach that efficiently captures global image features that might otherwise be lost in the splitting process. We evaluate the performance of our model for the generation of N-body samples using various statistical measures commonly used in cosmology. Our results show that the proposed model produces samples of high visual quality, although the statistical analysis reveals that capturing rare features in the data poses significant problems for the generative models. We make the data, quality evaluation routines, and the proposed GAN architecture publicly available at <https://github.com/nperraud/3DcosmoGAN>.

Keywords: generative models; cosmological simulations; Nbody simulations; generative adversarial network; fast cosmic web simulations; scalable GAN; multi-dimensional images

1 Introduction

The recent advances in the field of deep learning have initiated a new era for generative models. Generative Adversarial Networks (GANs) [1] have become a very popular approach by demonstrating their ability to learn complicated representations to produce high-resolution images [2]. In the field of cosmology, high-resolution simulations of matter distribution are becoming increasingly important for deepening our understanding of the evolution of the structures in the universe [3–5]. These simulations, made using the *N-body* technique, which represents the distribution of matter in 3D space by trillions of particles. They very slow to run and computationally expensive, as they evolve the positions of particles over cosmic time in small time intervals. Generative models have been proposed to emulate this

type of data, dramatically accelerating the process of obtaining new simulations, after the training is finished [6, 7].

N-body simulations represent the matter in a cosmological volume, typically between 0.1 - 10 Gpc, as a set of particles, typically between 100^3 to 2000^3 . The initial 3D positions of the particles are typically drawn from a Gaussian random field with a specific power spectrum. Then, the particles are displaced over time according to the laws of gravity, properties of dark energy, and other physical effects included in the simulations. During this evolution, the field is becoming increasingly non-Gaussian, and displays characteristic features, such as halos, filaments, sheets, and voids [8, 9].

N-body simulations that consist only of dark matter effectively solve the Poisson’s equation numerically. This process is computationally expensive, as the forces must be recalculated in short time intervals to retain the precision of the approximation. This leads to the need for frequent up-

*Correspondence: nathanael.perraudin@sdsc.ethz.ch

¹Swiss Data Science Center, ETH Zurich, Universitätstrasse 25, 8006 Zurich, Switzerland

Full list of author information is available at the end of the article

dates of the particle positions. The speed of these simulations is a large computational bottleneck for cosmological experiments, such as the Dark Energy Survey^[1], Euclid^[2], or LSST^[3].

Recently, GANs have been proposed for emulating the matter distributions in two dimensions [6, 7]. These approaches have been successful in generating data of high visual quality, and almost indistinguishable from the real simulations to experts. Moreover, several summary statistics often used in cosmology, such as power spectra and density histograms, also revealed good levels of performance. Some challenges still remain when comparing sets of generated samples. In both works, the properties of sets of generated images did not match exactly; the covariance matrix of power spectra of the generated maps differed by order of 10% with the real maps.

While these results are encouraging, a significant difficulty remains in scaling these models to generate three-dimensional data, which include several orders of magnitude more pixels for a single data instance. We address this problem in this work. We present a publicly available dataset of N-body cubes, consisting of 30 independent instances. Due to the fact that dark matter distribution is homogeneous and isotropic, and that the simulations are made using periodic boundary condition, the data can be easily augmented through shifts, rotations, and flips. The data is in the form of a list of particles with spatial positions x, y, z . It can be pixelised into 3D histogram cubes, where the matter distribution is represented in density voxels. Each voxel contains the count of particles falling into it. By publishing the N-body data and the accompanying codes we aim to encourage the development of large scale generative models capable of handling such data volumes.

We present a benchmark GAN system to generate 3D N-body voxel cubes. Our design of the novel GAN architecture scales to volumes of 256^3 voxels. Our proposed solution relies on two key building blocks. First, we split the generation of the high-dimensional data into smaller patches. Instead of assuming that the distribution of each patch is independent of the surrounding context, we model it as a function of the neighboring patches. Although splitting the generation process into patches provides a scalable solution to generate images of arbitrary size, it also limits the field of view of the generator, reducing its ability to learn global image features. The second core idea of our method addresses this problem by relying on a multi-scale approach that efficiently captures global dependencies that might otherwise be lost in the splitting process.

Our results constitute a baseline solution to the challenge. While the obtained statistical accuracy is currently insufficient for a real cosmological use case, we achieve two

goals: (i) we demonstrate that the project is tractable by GAN architectures, and (ii) we provide a framework for evaluating the performance of new algorithms in the future.

1.1 Related work

Generative models that produce novel representative samples from high-dimensional data distributions are increasingly becoming popular in various fields such as image-to-image translation [10], or image in-painting [11] to name a few. There are many different deep learning approaches to generative models. The most popular ones are Variational Auto-Encoders (VAE) [12], Autoregressive models such as PixelCNN [13], and Generative Adversarial Networks (GAN) [1]. None of these approaches scale to images of arbitrarily large size. PixelCNN [13] can scale to some extent, but this approach is slow to generate samples, as it builds the output image pixel-by-pixel in a sequential manner. We take inspiration from PixelCNN to design a patch-by-patch approach, rather than a pixel-by-pixel approach, which significantly speeds up the generation of new samples.

As mentioned above, splitting the generation process into patches reduces the ability of the generator to learn global image features. Some partial solutions to this problem can already be found in the literature, such as the Laplacian pyramid GAN [14] that provides a mechanism to learn at different scales for high quality sample generation, but this approach is not scalable as the sample image size is still limited. Similar techniques are used in the problem of super-resolution [15–17]. Recently, progressive growing of GANs [2] have been proposed to improve the quality of the generated samples and stabilize the training of GANs. The size of the samples produced by the generator is progressively increased by adding layers at the end of the generator and at the beginning of the discriminator. In the same direction, [18, 19] achieved impressive quality in the generation of large images by leveraging better optimization. Problematically, the limitations of the hardware on which the model is trained occur after a certain increase in size and all of these approaches will eventually fail to offer the scalability we are after.

GANs were proposed for generating of matter distributions in 2D. A generative model for the projected matter distribution, also called a *mass map*, was introduced by [7]. Mass maps are cosmological observables, as they are reconstructed by techniques such as, for example, gravitational lensing [20]. Mass maps arise through integration of the matter density over the radial dimension with a specific, distance-dependent kernel. The generative model presented in [7] achieved very good agreement with the real data several important non-Gaussian summary statistics: power spectra, density histograms, and Minkowski functionals [21]. The distributions of these summaries between sets of generated and real data also agreed well. However,

^[1]www.darkenergysurvey.org

^[2]www.euclid-ec.org

^[3]www.lsst.org

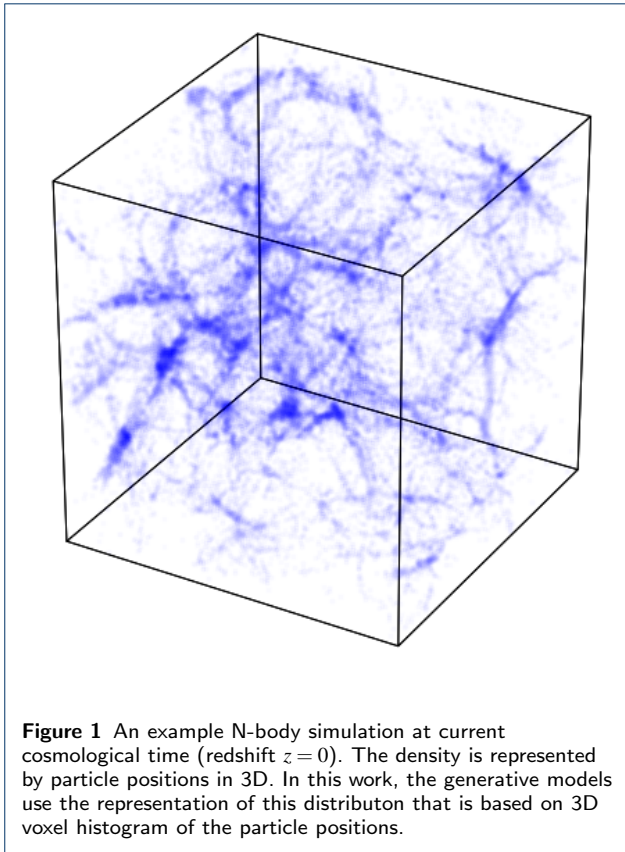


Figure 1 An example N-body simulation at current cosmological time (redshift $z = 0$). The density is represented by particle positions in 3D. In this work, the generative models use the representation of this distribution that is based on 3D voxel histogram of the particle positions.

the covariance matrix of power spectra within the generated and real sets did not match perfectly, differing by the order of 10%.

A generative model working on 2D slices from N-body simulations was developed by [6]. N-body slices have much more complex features, such as filaments and sheets, as they are not averaged out in projection. Moreover, the dynamic range of pixel values spans several orders of magnitude. GANs presented by [6] also achieved good performance, but only for larger cosmological volumes of 500 Mpc. Some mismatch in the power spectrum covariance was also observed.

Alternative approaches to emulating cosmological matter distributions using deep learning have been recently proposed. Deep Displacement Model [22] uses a U-shaped neural network that learns how to modify the positions of the particles from initial conditions to a given time in the history of the universe.

Generative models have also been proposed for solving other problems in cosmology, such as generation of galaxies [23], adding baryonic effects to the dark matter distribution [24], recovery of certain features from noisy astrophysical images [25], deblending galaxy superpositions [26], improving resolution of matter distributions [27].

2 The N-body data

2.1 Cosmological N-body simulations

The distribution of matter, dark matter and other particles in the universe at large scale, under the influence of gravity, forms a convoluted network-like structure called the cosmic web [8, 9, 28, 29]. This distribution contains information vital to the study of dark matter, dark energy, and the very laws of gravity [30–32]. Simulations of these various computational cosmological models [4, 33] lead to understanding of the fundamentals of cosmological measurements [34, 35], and other properties of the universe [3]. These simulations are done using N-body techniques. N-body techniques simulate the cosmic web using a set of particles in three dimensional space, and evolve their positions with time. This evolution is governed by the underlying cosmological model and the laws of gravity. The end result of an N-body simulation is the position of billions of particles in space, as depicted in Figure 1. Unfortunately, N-body simulations are extremely resource intensive, as they require days, or even weeks of computation to produce them [36, 37]. Moreover, a large number of these N-body simulations is needed to obtain good statistical accuracies, which further increases the computational requirements.

This computational bottleneck opens up a leeway for deep learning and generative models to offer an alternative solution to the problem. Generative models have the potential to be able to learn the underlying data distribution of the N-body simulations using a seed set of N-body samples to train on.

There are multiple techniques for running N-body simulations, which agree well for large scales, but start to diverge for small scales, around wavenumber $k = 1 \text{ Mpc}^{-1}$ [38]. Moreover, baryonic feedback can also affect the small scale matter distribution [39–41], and large uncertainty remains for these scales.

2.2 Data preprocessing

We produce samples of the cosmic web using standard N-body simulation techniques. We used L-PICOLA [42] to create 30 independent simulations. The cosmological model used was Λ CDM with Hubble constant $H_0 = 500h = 350 \text{ km/s/Mpc}$ ^[4], dark energy density $\Omega_\Lambda = 0.724$ and matter density $\Omega_m = 0.276$. We used the particle distribution at redshift $z = 0$. The output of the simulator is a list of particles $1,024^3$ 3D positions. To obtain the matter distribution, we first convert it to a standard 256^3 3D cube using histogram binning. We consider these cubes as the raw data for our challenge and can be downloaded at <https://zenodo.org/record/1464832>. The goal is to build a generative model able to produce new 3D histograms. While 30 samples might seem as a low number of

^[4]For cosmological scale, the distance is measured in megaparsec (Mpc) ($1 \text{ Mpc} = 3.3 \times 10^6 \text{ light-years}$).

samples to train a deep neural network, each sample contains a large number of voxels. One can also expand the training data by relying on data augmentation, using various rotations and circular translations as described in Appendix B. Problematically, the dynamic range of this raw data spans several orders of magnitude and the distribution is skewed towards smaller values, with a very elongated tail towards the larger values. Empirically, we find that this very skewed distribution makes learning a generative model difficult. Therefore, we first transform the data using a logarithm-based function, as described in Appendix A. Note that this transform needs to be inverted before the evaluation procedure.

2.3 Evaluation procedure

Following [6], we evaluate the quality of the generated samples with three summary statistics commonly used in the field of cosmology.

- 1 **Mass histogram** is the average (normalized) histogram of the pixel value in the image. Note that the pixel value is proportional to the matter density.
- 2 **Power spectrum density** (or PSD) is the amplitude of the Fourier modes as a function of their frequency (the phase is ignored). Practically, a set of bins is defined and the modes of similar frequency are averaged together.
- 3 **Peak histogram** is the distribution of maxima in the density distribution, often called ‘‘peak statistics’’, or ‘‘mass function’’. Peaks capture the non-Gaussian features present in the cosmic web. This statistic is commonly used on weak lensing data [43, 44]. A peak is defined as a pixel greater than every pixel in its 2-pixels neighbourhood (24 pixels for 2D and 124 for 3D).

Other statistics such as Minkowski functionals, three point correlation functions, or phase distributions, could be considered. Nevertheless, we find that the three aforementioned statistics are currently sufficient to compare different generative models.

Distance between statistics We define a score that reflects the agreement of the 3 aforementioned cosmological measures. Problematically, the scalars forming the 3 vectors representing them have very different scales and their metrics should represent the relative error instead of the absolute one. For this reason, we first compute the logarithm (in base 10) of the computed statistics s . As all statistics are positive but not strictly positive, we add a small value ε before computing the logarithm, i.e., $s_{\log} = \log_{10}(s + \varepsilon)$. ε is set to the maximum value of the statistic averaged over all real samples divided by 10^5 .

At this point, the relative difference connects to the difference of the real and fake s_{\log} , i.e.: $s_{\log}^r - s_{\log}^f \approx \log_{10} \frac{s^r}{s^f}$. One could quantify the error using a norm, i.e.: $\|\mathbb{E}s_{\log}^r - \mathbb{E}s_{\log}^f\|$.

However, such a distance does not take into account second-order moments. Rather, we take inspiration from the Fréchet Inception Distance [45]. We start by modeling the real and fake log statistics s_{\log}^r, s_{\log}^f as two multivariate Gaussian distributions. This allows us to compute the Fréchet Distance (FD) between the two distributions [46], which is also the Wasserstein-2 [47]. The FD between two Gaussian distribution with mean and covariance (m^r, C^r) and (m^f, C^f) is given by [48]:

$$d^2((m^r, C^r), (m^f, C^f)) = \|m^r - m^f\|_2^2 + \text{Tr}(C^r + C^f - 2C^r C^f) \quad (1)$$

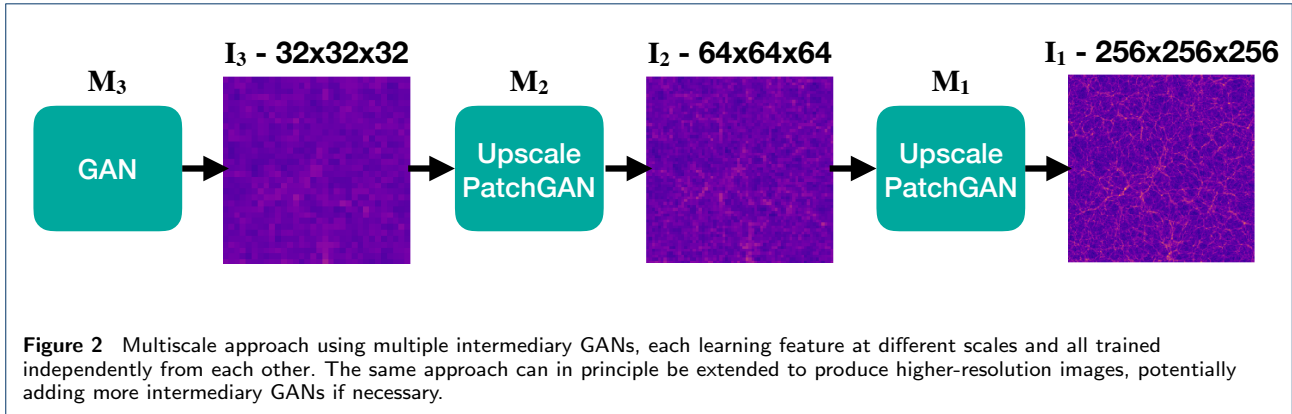
Note that [48] also proves that $\text{Tr}(C^r + C^f - 2C^r C^f)$ is a metric for the space of covariance matrices. We choose the FD over the Kullback-Leibler (KL) divergence for two reasons: a) the Wasserstein distance is still an appropriate distance when distributions have non-overlapping support and b) the KL is computationally more unstable since the covariance matrices need to be inverted.

2.4 N-body mass map generation challenge

Using the FD, we define a *score* for each statistic as

$$S^* = \frac{1}{d^2((m^r, C^r), (m^f, C^f))}, \quad (2)$$

where m, C are computed on the log statistics, i.e.: $\mathbb{E}s_{\log}^r = m^r$, $\mathbb{E}s_{\log}^f = m^f$. Along with this manuscript, we release our dataset and our evaluation procedure in the hope that further contributions will improve our solution. All information can be found at <https://github.com/nperraud/3DCosmoGAN>. We hope that this dataset and evaluation procedure can be a tool for the evaluation for GANs in general. Practically, these cosmological statistics are very sensitive. We observed two important properties of this problem. Firstly, a small variation in the generated images still has an impact on the statistics. The statistics can be highly affected by high density regions of the N-body data, and these regions are also the most rare in the training set. Secondly, while mode collapse may not directly affect the mean of the statistics, it can affect their second order moment significantly. We observed that obtaining a good statistical agreement (and hence a high score), is much more difficult than obtaining generating images that are indistinguishable for the human eye, especially for the 2-dimensional case. We found that the problems of high data volume, large dynamic range of the data, and strict requirement on good agreement in statistical properties of real and generated samples, pose significant challenge for generative models. We provide in Appendix E some baseline scores for the 2D case. The scores for the 3D case are reported in Section 5.



3 Generative Adversarial Networks (GANs)

Generative Adversarial Networks (GAN) are a particular class of generative models introduced by [1]. They are motivated by game theory and rely on two competing neural networks that are trained simultaneously: the generator G , which produces new samples, and the discriminator D , which attempts to distinguish them from the real ones. During training, it is the generator’s objective to fool the discriminator, while the discriminator resists by learning to discriminate real and fake data accurately. Eventually, if the optimization process is carried out successfully, the generator should improve to the point that its generated samples become indistinguishable from the real one. More formally, the generator G and the discriminator D play a minimax game that can be formulated as the following objective:

$$\min_G \max_D \mathbb{E}_{\mathbf{x} \sim \mathbb{P}_r} [\log D(\mathbf{x})] + \mathbb{E}_{\tilde{\mathbf{x}} \sim \mathbb{P}_g} [\log (1 - D(\tilde{\mathbf{x}}))], \quad (3)$$

where \mathbb{P}_r is the data distribution and \mathbb{P}_g is the generator distribution implicitly defined by $\tilde{\mathbf{x}} = G(z), z \sim p(z)$. The latent variable z is sampled from some simple prior distribution p , e.g., a uniform or a Gaussian distribution.

According to [1], if the discriminator is trained optimally, i.e., the global maximum over D is reached, then minimizing eq. (3) with respect to the generator parameters is equivalent to minimizing the Jensen-Shannon divergence between \mathbb{P}_r and \mathbb{P}_g . In practice, the global maximum is never attained and the discriminator parameters are updated a fix number of times between each update of the generator update (gradient step).

Numerous variants of the original GAN approach have been proposed, many of them aiming to improve stability including e.g. [49–51]. In our work, we rely on the improved Wasserstein GAN approach introduced in [50]. The latter optimizes the Wasserstein distance instead of the Jensen-Shannon divergence and penalizes the norm of gradient of the critic instead of using a hard clipping as in

the original Wasserstein GAN [51]. The resulting objective function is

$$\min_G \max_{D \in \mathcal{D}} \mathbb{E}_{\mathbf{x} \sim \mathbb{P}_r} [D(\mathbf{x})] - \mathbb{E}_{\tilde{\mathbf{x}} \sim \mathbb{P}_g} [D(\tilde{\mathbf{x}})] + \lambda \mathbb{E}_{\hat{\mathbf{x}} \sim \mathbb{P}_{\hat{\mathbf{x}}}} [(\|\nabla_{\hat{\mathbf{x}}} D(\hat{\mathbf{x}})\|_2 - 1)^2], \quad (4)$$

where $\mathbb{P}_{\hat{\mathbf{x}}}$ is defined implicitly by sampling uniformly along straight lines between pair of points sampled from the true data distribution \mathbb{P}_r and the generator distribution \mathbb{P}_g . The weight λ is the penalty coefficient.

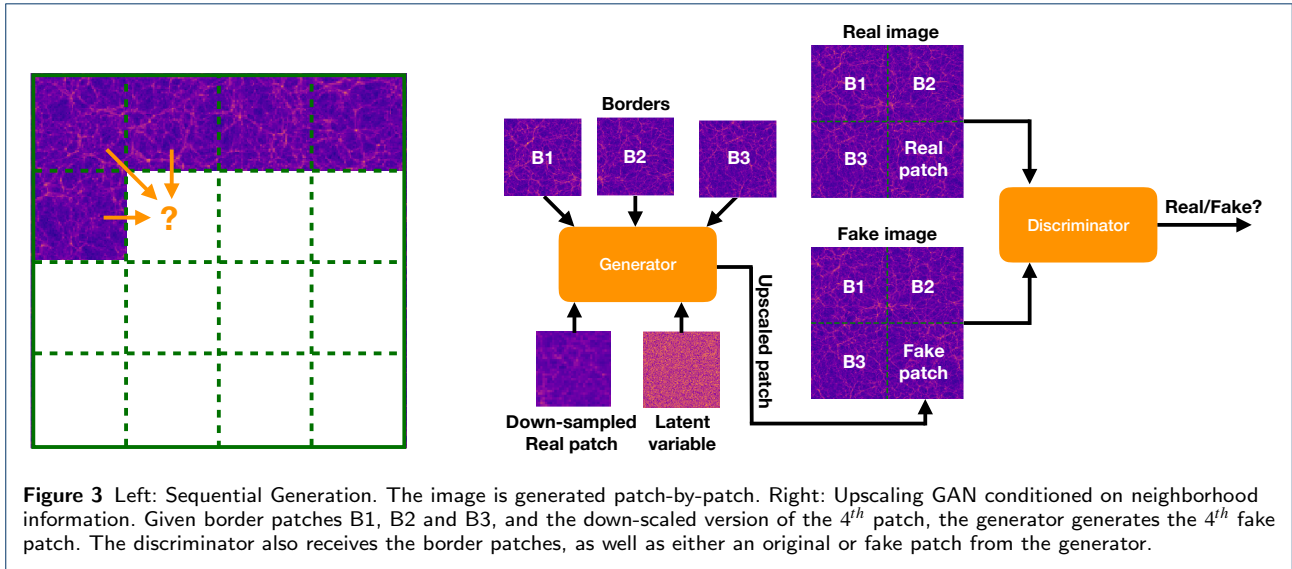
4 GAN-sequence approach

We propose a novel approach to allow efficient learning of a GAN model for 2D and 3D images of arbitrary size. Our method relies on two building blocks: 1) a multi-scale model that improves the quality of the generated samples, both visually and quantitatively, by learning unique features at different scales, and 2) a training strategy that enables learning images of arbitrary size, that we call “conditioning on neighborhood”.

4.1 Multi-scale Model

Our multi-scale approach is inspired by the Laplacian pyramid GAN [14]. We refer to three image types of different sizes, namely $I_3 = 32 \times 32 \times 32$, $I_2 = 64 \times 64 \times 64$, $I_1 = 256 \times 256 \times 256$ ^[5] pixels, where I_2 is a down-scaled version of I_1 and I_3 is a down-scaled version of I_2 . The multi-scale approach is shown in figure 2 and uses three different GANs, M_1 , M_2 and M_3 , all trained independently from each other, and can therefore be trained in parallel. We train GAN M_3 to learn the data distribution of images I_3 , while the GANs M_2 and M_1 are conditioned on the images produced by M_3 and M_2 , respectively. In our implementation, we take M_3 to be a normal Deep Convolution GAN (DCGAN) that learns to produce down-scaled samples of

^[5]We will use the abbreviations 32^3 , 64^3 and 256^3 for conciseness.

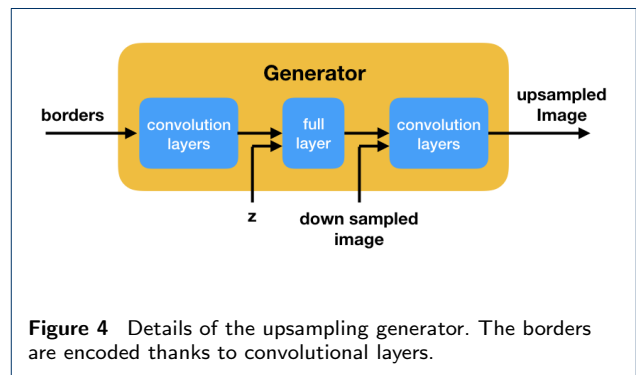


size I_3 . We design GANs M_2 and M_1 to have the following properties: 1) they produce outputs using a sequential patch-by-patch approach and 2) the output of each patch is conditioned on the neighboring patches. This procedure allows handling of high data volume, while preserving the long-range features in the data. Moreover, different GANs learn salient features at different scales, which contribute to an overall improved quality of the samples produced the final GAN M_1 . Further details regarding the implementation details are provided in Appendix F.

4.2 Conditioning on Neighborhoods

The limited amount of memory available to train a GAN generator makes it impractical to directly produce large image samples. Using current modern GPUs with 16Gb of RAM and a state-of-the-art network architecture, the maximum sample size we were allowed to use was 32^3 , which is far from our target taken to be 256^3 . In order to circumvent this limitation, we propose a new approach that produces the full image (of size 256^3) patch-by-patch, each patch being of smaller size (32^3 in our case). This approach is reminiscent of the Pixel-CNN [13], where 2D images are generated pixel-by-pixel, rather than the entire picture being generated at once. Instead of assuming that the distribution of each patch is independent of the surrounding context, we model it as a function of the neighboring patches. The generation process is done using a raster-scan order, which implies that a patch depends on the neighboring patches produced before the current patch. The process illustrated in Figure 3 is for the 2D case with three neighboring patches; the generalization to three dimensions is straightforward as it simply requires seven neighboring 3D patches.

In the generator, the neighborhood information, i.e. the borders, is first encoded thanks to a few convolutional layers. Then it is concatenated with the latent variable and en-



ter a fully connected layer and are reshaped into a 3D image. At this point, the down-sampled version of the image is concatenated. After a few extra convolutional layers, the generator produces the lowest rightmost patch with the aim of making it indistinguishable to the patch from the real data. The generator architecture is detailed in Figure 4. In the case where there is no neighborhood information available, such as at the boundary of a cube, we pad with zeros. The discriminator is given images containing four patches where the lower right patch is either the real data or the fake data generated by the generator. The generator only produces patches of size 32^3 , irrespective of the size of the original image. This way this method can scale to any image size, which is a great advantage. The discriminator only has access to a limited part of the image and ignores the long-range dependencies. This issue, however, is handled by the multi-scale approach described in the previous section. We actually tried a model only conditioned on the neighborhoods as detailed in Appendix C. It ended up performing significantly worse than using the multi-scale approach.

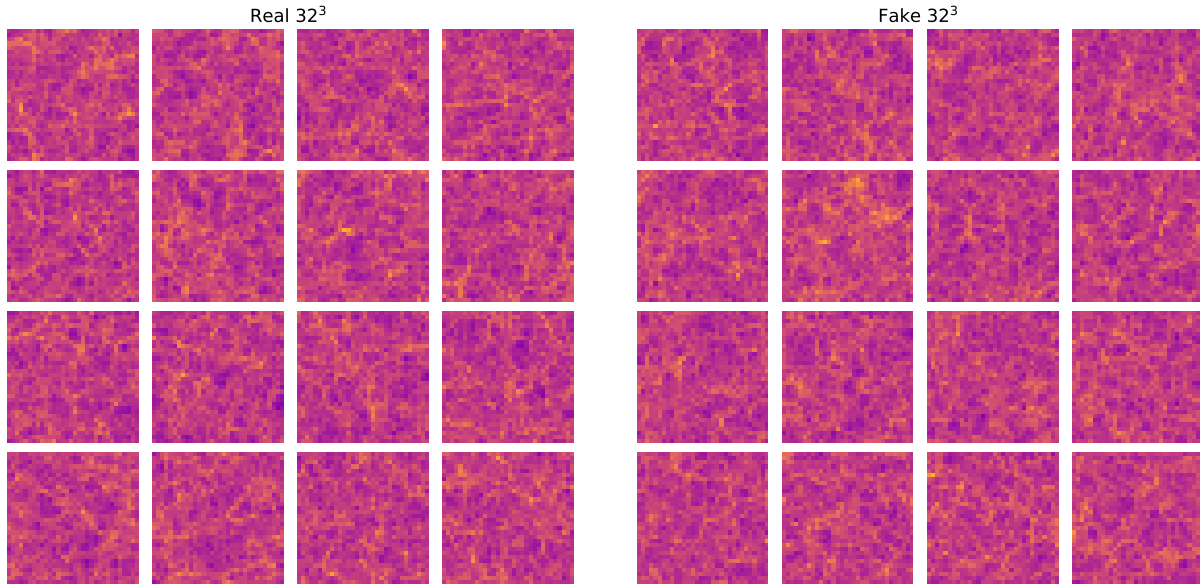


Figure 5 8-down-scaled sample generation (32^3 cubes). Middle slice from 16 real and 16 fake WGAN M_3 samples. Video: <https://youtu.be/uLwrF73wX2w>

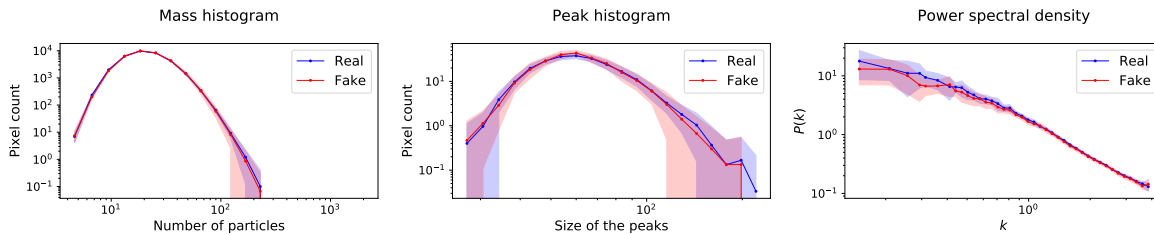


Figure 6 Statistics of the 8-downscaled 32^3 cubes. The fake samples are generated from WGAN M_3 . The power spectrum density is shown in units of $h \text{ Mpc}^{-1}$, where $h = H_0/100$ corresponds to the Hubble parameter.

5 Experimental results

Implementation details We used python and Tensorflow to code the models which are trained on GPUs with 16Gb of memory. The batch size is set to 8 for all the experiments. The optimization algorithm is always RMS Prop [52] with a learning rate of $3 \cdot 10^{-5}$ for all the experiments. All the GANs are WGANs with a Gaussian prior distribution. The neural networks used in our experiments are variants of deep convolutional networks with inception modules and/or residual connections. Additional details are available in Appendix F.

First Up-scale (Latent Code to I_3) The WGAN M_3 is a traditional convolution WGAN with kernels of size $4 \times 4 \times 4$, where both the generator and the discriminator have 5 deconvolution/convolution layers. We use leaky Relu non-linearity. The architecture is detailed in Table 3 of the appendix.

Figure 5 shows the middle slice from 16 samples $3D I_3$ drawn from the generator of the WGAN M_3 compared to the equivalent slices from real samples. In Figure 6, we

plot our evaluation statistics for 30 samples. We use only 30 samples as it is our initial number of histograms in the dataset. Both from a visual and from a statistical point of view the generated samples drawn from M_3 are generally similar to the true data, we only find a slight disagreement at higher frequencies. Note that the low number of samples and the size of each of them does not allow us to compute very accurate statistics, hence limiting our evaluation.

Second Up-scale (I_3 to I_2) The WGAN M_2 is a conditional convolution WGAN with an encoder of 3 convolution layers for the borders. The the rest of the network is similar to M_3 (see Table 4 of the appendix). The sample images and summary statistics shown in the appendix indicate that the samples differ slightly from the true data at higher frequencies. Nevertheless, we will observe later on that this small disagreement does not significantly impact the final statistics of the multi-scale approach.

To visualize the quality of up-scaling achieved by our first up-sampling cell independently from the rest of the pipeline, we first down-scale a real 256^3 cube to 32^3 , and

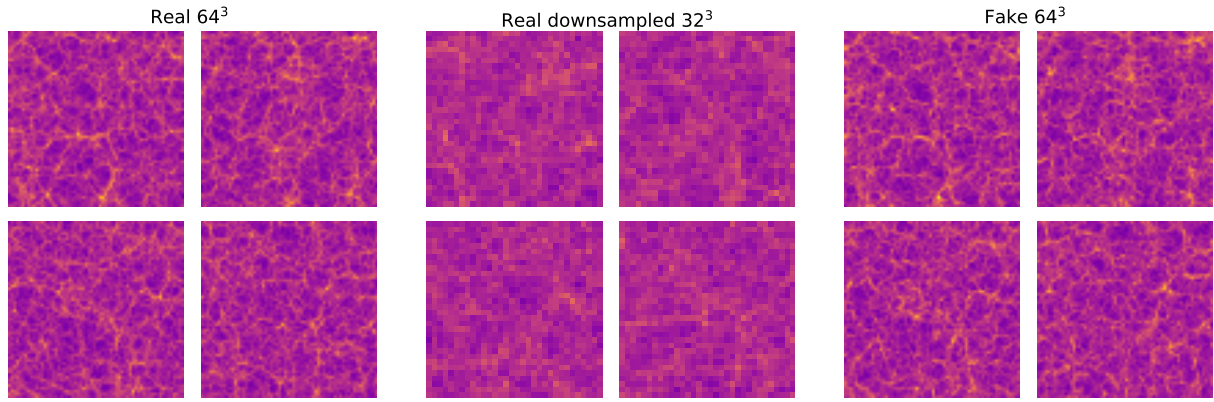


Figure 7 Up-scaling a 32^3 cube to 64^3 . Left and right: middle slices from 4 real and fake 64^3 samples. The fake is generated by conditioning the WGAN M_2 on the real down-scaled 32^3 cube (center). Video: <https://youtu.be/IIPoK8s1SHU>

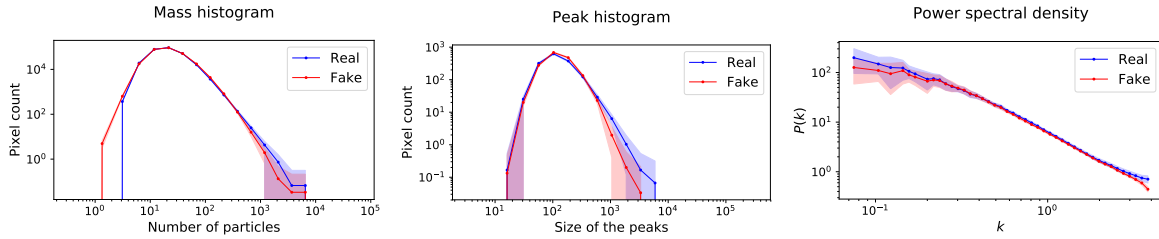


Figure 8 Statistics of the samples produced by M_2 . The fake samples are generated by conditioning WGAN M_2 on the real down-scaled 32^3 samples. The power spectrum density is shown in units of $h \text{ Mpc}^{-1}$, where $h = H_0/100$ corresponds to the Hubble parameter.

then provide it as input I_3 to the WGAN M_2 . We then observe the result of the up-scaling to 64^3 . Figure 7 shows a few slices from a 3D fake I_2 sample, alongside the real down-scaled I_3 image and the real I_2 image. We observe a clear resemblance between the up-scaled fake sample and the real sample. The statistics of this layer are displayed in Figure 8 and Figure 8. We observe a dissimilarity for rare features, such as very massive peaks. This can be explained by the fact that it is very difficult for GANs in general to capture correctly the statistics of very rare features. We also note that the final statistics after the whole pipeline match better than the one of this particular cell.

Final Up-scale (I_2 to I_1) The WGAN M_1 is a Deep Convolution WGAN with inception modules [53]. The inception modules have filters of three different sizes: $1 \times 1 \times 1$, $2 \times 2 \times 2$ and $4 \times 4 \times 4$. The input tensor is convolved with all three types of filters, using padding to keep the output shape the same as the input shape. The outputs of the convolution of the input tensor with each of the 3 filters are concatenated along the channel axis, to give the final output of the inception module. The generator and discriminator have 8 and 6 inception layers respectively.

To visualize the quality of up-scaling achieved by our second up sampling cell, we repeat the same process. We

down-scale real 256^3 cubes to 64^3 and feed them as input to WGAN M_1 . Figure 9 shows the middle slices of 2 real and fake I_1 sample. The fake samples are generated from WGAN M_1 . Although, the up-sampling factor is 4, the WGAN M_1 is able to produce convincing samples with sufficient high frequencies. We also note the similarity between the statistics displayed in Figure 10 and the Figure 12 of the full pipeline. This suggests that the last layer of our pipeline may be the most important one in this regard.

Full Multi-scale Pipeline Now that we have all three WGANs trained, we use them to generate fake I_1 samples (Sampling details are given in Appendix D). Figure 11 shows a few slices from a 3D fake I_1 image generated using the full pipeline, alongside a random real I_1 image. Figure 12 shows the summary statistics of 500 GAN generated samples, compared to that of real samples. The visual agreement between the real and generated samples is good, nevertheless the trained human eye can still distinguish between real and fake samples. In particular, a careful visualization reveals that the transitions between the different patches is still imperfect and that there are less long range filaments. The summary statistics agree very well for the middle range of mass density, with slight disagreement at the extremes. The shape of the power spectrum density (PSD) matches well, but overall amplitude is too high for

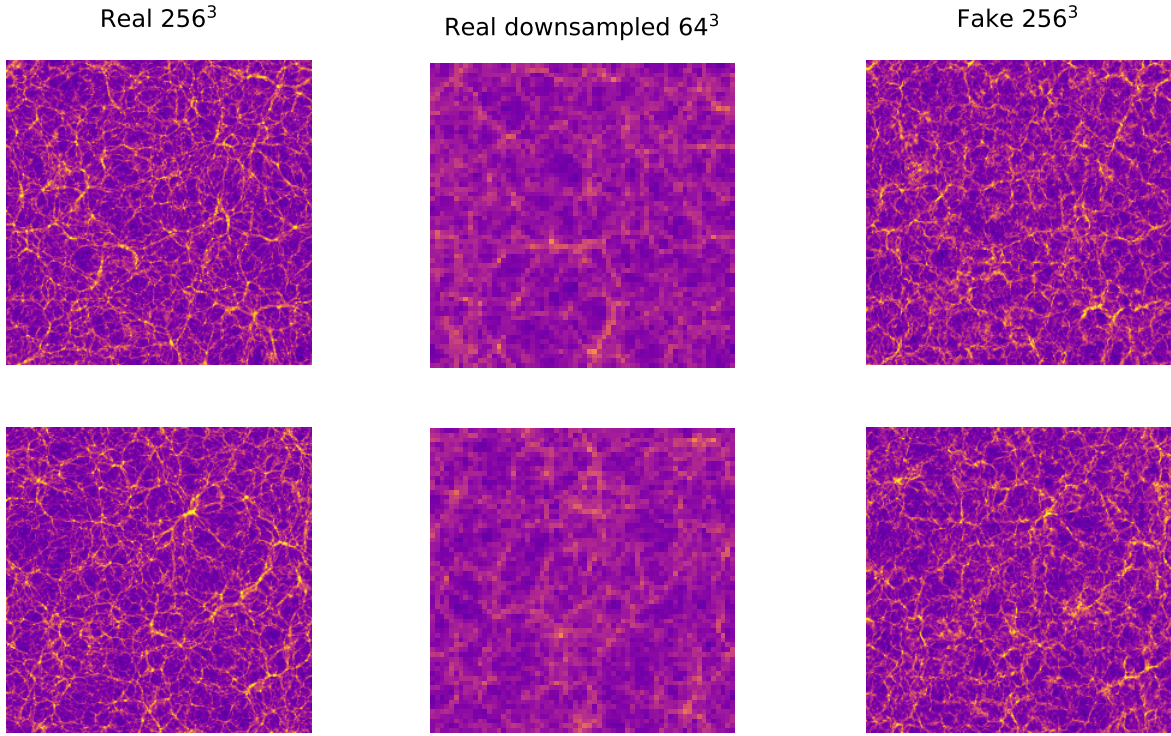


Figure 9 Upsampling a 64^3 cube to 256^3 . Left and right: middle slices from 2 real and fake 256^3 samples. The WGAN M_1 that generates the fake sample is conditioned on the real image down-scaled to 64^3 (center). Video:

<https://youtu.be/guUYP8Z0oVU>

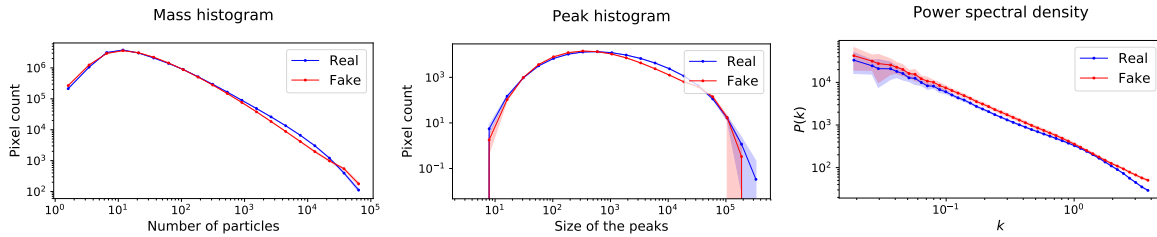


Figure 10 Statistics for the WGAN M_1 producing fake 256^3 cubes. The fake samples are generated by conditioning WGAN M_1 on the real cube down-scaled to 64^3 . The power spectrum density is shown in units of $h \text{ Mpc}^{-1}$, where $h = H_0/100$ corresponds to the Hubble parameter.

	PSD	Mass Hist.	Peak Hist
Fréchet Distance d^2	0.36	0.17	1.58
Score S^*	2.72	5.72	0.63
Reference score S^*	8.16	1433	8.17

Table 1 Scores computed for the 30 GAN-generated 256^3 images using the full multi-scale pipeline. We refer to (2) and (1) for details. The reference is computed by comparing two sets of 15 real samples. It represent the best score that can be achieved.

most of the k range. Eventually, Table 1 present the scores obtained for the 30 cubes of size 256^3 using the full multi-scale pipeline as generated by the full GAN sequence.

6 Conclusion

In this work we introduce a new benchmark for the generation of 3D N-body simulations using deep generative models. The dataset is made publicly available and contains matter density distributions represented as cubes of $256 \times 256 \times 256$ voxels. While the performance of the generative model can be measured by visual inspection of the generated samples, as commonly done on datasets of natural images, we also offer a more principled alternative based on a number of summary statistics that are commonly used in cosmology. Our investigation into this problem has revealed that several factors make this task challeng-

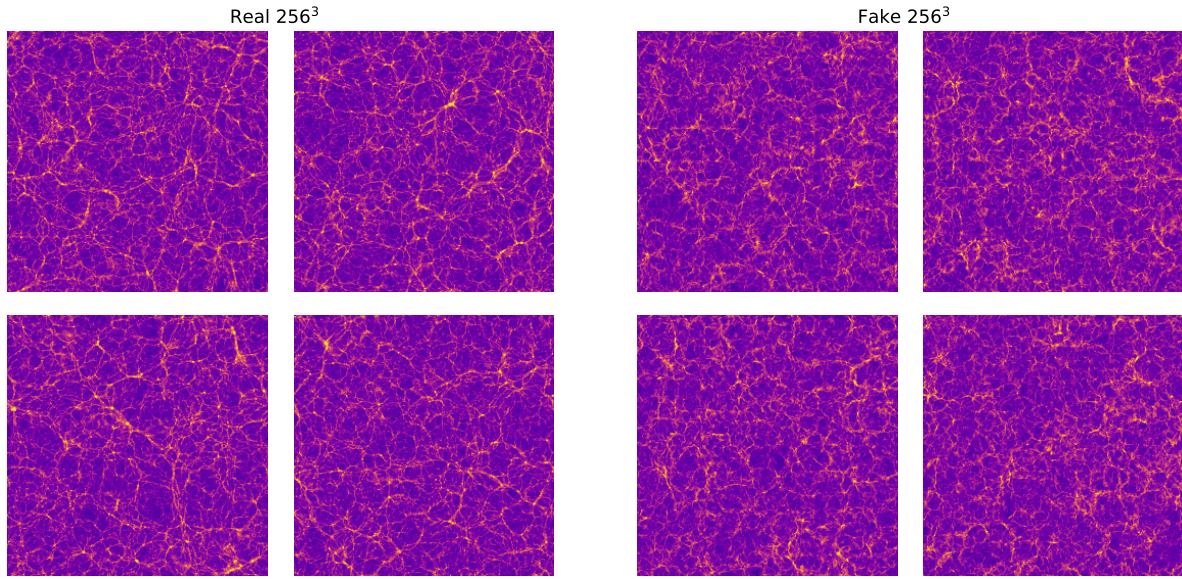


Figure 11 Middle slice from real and generated 256^3 samples. The GAN-generated samples are produced using the full multi-scale pipeline. Videos:

- 32-scale: <https://youtu.be/uLwrF73wX2w>
- 64-scale: <https://youtu.be/xI2cUuk3DRc>
- 256-scale: <https://youtu.be/nWXP6DVEa1A>

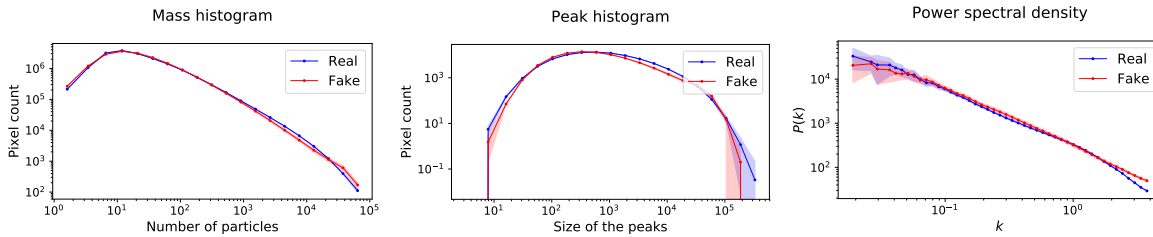


Figure 12 Summary statistics of real and GAN-generated 256^3 images using the full multi-scale pipeline. The power spectrum density is shown in units of $h \text{ Mpc}^{-1}$, where $h = H_0/100$ corresponds to the Hubble parameter.

ing, including: (i) the sheer volume of each data sample, which is not straightforwardly tractable using conventional GAN architectures, (ii) the large dynamic range of the data that spans several orders of magnitude; which requires a custom-designed transformation of the voxel values, and (iii) the need for high accuracy required for the model to be practically useable for a real cosmological study. Adding to the difficulties of (i) and (ii), this also requires accurately capturing features that are rare in the training set.

As a first baseline result for the newly introduced benchmark, we proposed a new method to train a deep generative model on 3D images. We split the generation process into the generation of smaller patches as well as condition on neighboring patches. We also apply a multi-scale approach to learn multiple WGANs at different image resolutions, each capturing salient features at different scales. This approach is inspired by Laplacian pyramid GAN [14] and by

PixelCNN [13], which have both been developed for 2D data.

We find that the proposed baseline produces N-body cubes with good visual quality compared to the training data, but significant differences can still be perceived. Overall, the summary statistics between real and generated data match well, but notable differences are present for high voxel values in the mass and peak histograms. The power spectrum has the expected shape, with amplitude that is too high for most of the k values. The overall level of agreement is promising, but can not yet be considered as sufficient for practical applications in cosmology.

In our current model, the discriminator only has access to a partial view of the final image. The dependencies at small scale that may exist between distant patches are therefore not captured by the discriminator. Extending this model to allow the discriminator to have a more global view would be the next logical extension of this work. We have also

observed empirically that the extreme right tail of the histogram is often not fully captured by the generator. Designing architectures that would help the generative model to handle large dynamic range in the data could further improve performance. One could also get further inspiration from the literature on generative models for video data, such as [54–56]. Given the observations made in our experiments, one might for instance expect that the two stage approach suggested in [56] could address some of the problem seen with the right tail of the distribution.

As a further direction, it should be possible to condition the generation as a function of cosmic time or cosmological parameters. To do so, a conditional GAN model can be developed, as in [57], where the samples are generated as a function of cosmic time or cosmological parameters.

Appendix A: Input Data Transformation

The general practice in machine learning is that the input data is first standardized before giving it to any machine learning model. This preprocessing step is important as many neural networks and optimization blocks are scale-dependent, resulting in most architectures working optimally only when the data is appropriately scaled. Problematically, because of the physical law of gravity, most of the universe is empty, while most of the matter is concentrated in a few small areas and filaments. The dataset had the minimum value of 0 and the maximum value of 185,874, with most of the voxels concentrated close to zero, and significantly skewed towards the smaller values and has an elongated tail towards the larger ones. Even with standardization, it is difficult for a generative model to learn very sparse and skewed distributions. Hence we transform the data using a special function, in a slightly different way than [6].

In order to preserve the sensitivity of the smaller values, a logarithm-based transformation function is a good candidate. Nevertheless, to maintain the sensitivity to the large values, we should favor a linear function. In our attempt to coincide the best of the two regimes, we design a function that is logarithmic for lower values and linear for large one, i.e after a specified cutoff value. The exact forward transformation function, $y = f(x, c, s)$ is defined as:

$$f(x, c, s) = f'(x + s, c) - f'(s, c), \quad (5)$$

where

$$f'(x, c) = \begin{cases} 3 \log_e(x + 1) & \text{if } x \leq c \\ 3(\log_e(c + 1) + \frac{x}{c} - 1) & \text{otherwise.} \end{cases} \quad (6)$$

As a result, the backward transformation function $x = b(y, c, s)$ reads

$$b(y, c, s) = b'(y + f'(s, c), c) - s, \quad (7)$$

where

$$b'(y, c) = \begin{cases} e^{\frac{y}{3}} - 1 & \text{if } y \leq 3 \log_e(c + 1) \\ c(\frac{y}{3} + 1 - \log_e(c + 1)) & \text{otherwise.} \end{cases} \quad (8)$$

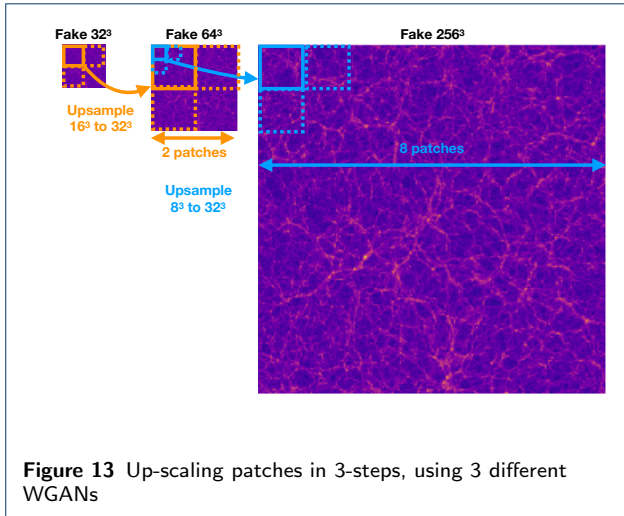
Here c and s are selected hyper-parameters. For our experiments we found $c = 20,000$ and $s = 3$ to be good candidates. After the forward transformation, the distribution of the data becomes similar to a one-sided Laplacian distribution. We always invert this transformation once new data is generated, before calculating the summary statistics.

Appendix B: N-body Training Set Augmentation

As N-body simulations are very expensive, we need to sure to use all the information available using an optimal dataset augmentation. To augment the training set, the cubes are randomly rotated by multiples of 90 degrees and randomly translated along one of the 3 axes. The cosmological principle states that the spatial distribution of matter in the universe is homogeneous and isotropic when viewed on a large enough scale. As a consequence there should be no observable irregularities in the large scale structure over the course of evolution of the matter field that was initially laid down by the Big Bang [58]. Hence, the rotational and translational augmentations do not alter the data distribution that we are trying to model in any way. Moreover, we note that use circular translation in our augmentation scheme. This is possible because N-body simulations are created using the *periodic boundary condition*: a particle exiting the box on one side enters it immediately on the opposite side. Forces follow the same principle. This prevents the particles from collapsing to the middle of the box under gravity. These augmentations are important given that we only have 30 N-body cubes in our training set.

Appendix C: Single scale model

In order to evaluate the effectiveness of the multi-scale approach, we compare our model to a uni-scale variant that is not conditioned on the down-sampled image. Given the 7 borders and some latent variable, the generator will simply produce the last corner. More simply, it is a direct implementation of the principle displayed in Figure 13 left. Note that the discriminator is not conditioned on the down-sampled image as well. An important issue with the uni-scale model is that the discriminator never see more than 64^3 pixels at once. Hence, it is likely to fail to capture long-range correlations. Practically, we observed that the training process is unstable and subject to mode collapse. The results are not included in this manuscript as they were of lesser quality. Nevertheless, we provide the code and the trained weights for this architecture as well.



	PSD	Mass Hist.	Peak Hist
32×32	9.24	7.44	3.25
64×64	5.08	5.56	1.09
128×128	5.27	4.37	0.89
256×256	3.36	5.66	1.22

Table 2 Scores computed for the generation of 2D images.

Appendix D: Sample Generation

At the inference time, the data pipeline is different than at the training time. First a latent variable is randomly drawn and feed into the M_3 which produce a 32^3 low-resolution cube. Then the up-sampling process of M_2 is performed. At first all borders are fed with zeros. Then the 64^3 image is built recursively (in 8 times) where the previously generated patches are re-feed as borders into the generator. When the image is completely up-sampled to 64^3 , it is fed into M_1 that up-sample it similarly to 256^3 . Note that this last step requires the generation of 8^3 patches. An illustration, adapted to the 2D case, is given in Figure 13.

Appendix E: 2-dimensional score baselines

We present here baseline scores for the generation of 2D images. We trained 4 different models corresponding to 4 different image sizes: 32^2 , 64^2 , 128^2 and 256^2 . We use a traditional convolutional Wasserstein GAN. The generated images are indistinguishable to the real one for the human eye. However statistics do not exactly match as the score of Table 2 indicates. The code and the architecture used to produce these results is available at <https://github.com/nperraud/3DcosmoGAN>.

Appendix F: Architecture details

For completeness, we provide here the detailed architectures used in our experiment. All Wasserstein GANs were trained with using a gradient penalty loss with $\gamma_{GP} = 10$, as described in [50]. We use RMSprop with a learning rate $3 \cdot 10^{-5}$ for both the generator and discriminator. The discriminator was updated 5 times per generator update. All

weights were initialized using Xavier Initializer, except the bias that was initialized to 0. We used leaky relu and spectral normalization [59] to stabilize the network. The architectures are detailed in Tables 3, 4 and 5.

Handling the input border is an architectural challenge as itself. We used two different solutions to overcome this issue and use 1 of them for each scale.

The specificities of the generator M_2 . The generator M_2 possesses a convolutional encoder for the borders. Once the borders are encoded, we concatenate them with the latent variable. The downsampled image simply concatenated at the first convolution layer (see Table 4).

The specificities of the generator M_1 . The generator M_1 does not possess an encoder, but utilize the border directly as extra channels. As a result, the generator convolution all have a stride of 1. The downsampled image is first upsampled using a simple deconvolution with a constant kernel and then concatenated as an input. The latent variable is of size 32^3 to avoid a memory consuming linear layer. Eventually, as the convolution is shift-invariant, we perform two transformations to the input borders before feeding them to the generator. As a results, we flip them to obtain a correct alignment with produced corner. Furthermore, to improve the capacity of the networks without increasing to much the number of parameters and channels, we use an inception inspired module. The module is simply composed of 3 convolutions ($1 \times 1 \times 1$, $2 \times 2 \times 2$, $4, 4, 4$) in parallel followed by a merging $1 \times 1 \times 1$ convolution. Finally, to further help the discriminator, we also feed some PSD estimation at the beginning of its linear layer (see Table 5).

Training stabilization using a regularizer. While it has been shown that the gradient penalty loss of the Wasserstein GAN helps in stabilizing the training process [50], this term does not prevent the discriminator to saturate. For example, when the discriminator has a high final bias, its output will be very large for both real and fake sample, yet its loss might be controlled as the output of real samples is subtracted from the one of the fake samples. In practice, we noticed that when this behavior was happening, the learning process of the generator was hindered and the produced samples were of worse quality. In order to circumvent this issue, we added a second regularization term:

$$\text{relu}(D_{real} \cdot D_{fake}) \quad (9)$$

Our idea was that the regularization should kick in only to prevent the in-desirable effect and should not affect the rest of the training. If the discriminator is doing a good job, then D_{real} should be positive and D_{fake} negative nullifying the regularization. On the contrary if both of these term are of the same sign, the output will be penalized quadratically

forcing it to remain close to 0. While the effect of this second regularization term is still unclear to us, it did help to stabilize our optimization procedure for the multi-scale approach.

As we release our code and entire pipeline, we encourage the reader to check it for additional details.

Operation	Parameter size	Output Shape
Generator		
Input $z \mathcal{N}(0,1)$		$(n, 256)$
Dense	$(256, 256d)$	$(n, 256d)$
Reshape		$(n, 4, 4, 4d)$
DeConv 3D (Stride 2)	$(4, 4, 4, 4d, 4d)$	$(n, 8, 8, 8, 4d)$
LReLU ($\alpha = 0.2$)		$(n, 16, 16, 16, 4d)$
DeConv 3D (Stride 2)	$(4, 4, 4, 4d, 2d)$	$(n, 16, 16, 16, 2d)$
LReLU ($\alpha = 0.2$)		$(n, 16, 16, 16, 2d)$
DeConv 3D (Stride 2)	$(4, 4, 4, d, d)$	$(n, 32, 32, 32, d)$
LReLU ($\alpha = 0.2$)		$(n, 32, 32, 32, 2d)$
DeConv 3D (Stride 1)	$(4, 4, 4, d, d)$	$(n, 32, 32, 32, d)$
LReLU ($\alpha = 0.2$)		$(n, 32, 32, 32, 2d)$
DeConv 3D (Stride 1)	$(4, 4, 4, d, 1)$	$(n, 32, 32, 32, 1)$
Discriminator		
Input generated image		$(n, 32, 32, 32, 1)$
Conv 3D (Stride 2)	$(4, 4, 4, 1, d)$	$(n, 32, 32, 32, d)$
LReLU ($\alpha = 0.2$)		$(n, 32, 32, 32, d)$
Conv 3D (Stride 2)	$(4, 4, 4, d, d)$	$(n, 32, 32, 32, d)$
LReLU ($\alpha = 0.2$)		$(n, 32, 32, 32, d)$
Conv 3D (Stride 1)	$(4, 4, 4, d, 2d)$	$(n, 16, 16, 16, 2d)$
LReLU ($\alpha = 0.2$)		$(n, 16, 16, 16, 2d)$
Conv 3D (Stride 1)	$(4, 4, 4, 2d, 4d)$	$(n, 8, 8, 8, 4d)$
LReLU ($\alpha = 0.2$)		$(n, 8, 8, 8, 4d)$
Conv 3D (Stride 1)	$(4, 4, 4, 4d, 8d)$	$(n, 4, 4, 4, 8d)$
LReLU ($\alpha = 0.2$)		$(n, 4, 4, 4, 8d)$
Reshape		$(n, 512d)$
Dense	$(512d, 1)$	$(n, 1)$

Table 3 Detailed architecture of the low resolution GAN $0 \rightarrow 32^3$. $d = 64$.

Abbreviations

- GAN: Generative adversarial networks
- DCNN: Deep convolutional neural networks
- LSST: Large Synoptic Survey Telescope
- CDM: Cold Dark Matter
- GPU: Graphics Processing Unit
- PSD: Power Spectral Density
- FD: Fréchet Distance
- KL: Kullback-Leibler

Declarations

Availability of data and material

The data and code to reproduce the experiment of this study are available at <https://github.com/nperraud/3DCosmoGAN> and <https://zenodo.org/record/1464832>.

Competing interests

The authors declare that they have no competing interests.

Funding

This work was supported by the Swiss Data Science Centre (SDSC), project *sd01 - DLOC: Deep Learning for Observational Cosmology*, and grant number 200021_169130 and PZ00P2_161363 from the Swiss National Science Foundation. The funding bodies had no involvement in the design of the study, collection, analysis, and interpretation of data, or writing the manuscript.

Operation	Parameter size	Output Shape
Generator		
Input borders		$(n, 32, 32, 32, 7)$
Conv 3D (Stride 2)	$(4, 4, 4, 7, d)$	$(n, 16, 16, 16, d)$
Conv 3D (Stride 2)	$(4, 4, 4, d, d)$	$(n, 8, 8, 8, d)$
Conv 3D (Stride 2)	$(4, 4, 4, d, 16)$	$(n, 4, 4, 4, 16)$
Reshape		$(n, 1024)$
Input $z_1 \mathcal{N}(0,1)$		$(n, 1024)$
Concatenation		$(n, 2048)$
Dense	$(2048, 256d)$	$(n, 256d)$
Reshape		$(n, 16, 16, 16, 2)$
Input downsampled corner		$(n, 16, 16, 16, 1)$
Input $z_2 \mathcal{N}(0,1)$		$(n, 16, 16, 16, 1)$
Concatenation		$(n, 16, 16, 16, 4)$
DeConv 3D (Stride 1)	$(4, 4, 4, 4, d)$	$(n, 16, 16, 16, d)$
LReLU ($\alpha = 0.2$)		$(n, 16, 16, 16, 4d)$
DeConv 3D (Stride 1)	$(4, 4, 4, d, d)$	$(n, 16, 16, 16, d)$
LReLU ($\alpha = 0.2$)		$(n, 16, 16, 16, 2d)$
DeConv 3D (Stride 2)	$(4, 4, 4, d, 4d)$	$(n, 32, 32, 32, 4d)$
LReLU ($\alpha = 0.2$)		$(n, 32, 32, 32, 4d)$
DeConv 3D (Stride 1)	$(4, 4, 4, 4d, 2d)$	$(n, 32, 32, 32, 2d)$
LReLU ($\alpha = 0.2$)		$(n, 32, 32, 32, d)$
DeConv 3D (Stride 1)	$(4, 4, 4, 2d, 1)$	$(n, 32, 32, 32, 1)$
Discriminator		
Input generated image		$(n, 32, 32, 32, 1)$
Input borders		$(n, 32, 32, 32, 7)$
Reshape to a cube		$(n, 64, 64, 64, 1)$
Input smooth image		$(n, 64, 64, 64, 1)$
Concatenation (+ diff)		$(n, 64, 64, 64, 3)$
Conv 3D (Stride 1)	$(4, 4, 4, 3, d)$	$(n, 64, 64, 64, d)$
LReLU ($\alpha = 0.2$)		$(n, 64, 64, 64, d)$
Conv 3D (Stride 2)	$(4, 4, 4, d, 2d)$	$(n, 32, 32, 32, 2d)$
LReLU ($\alpha = 0.2$)		$(n, 32, 32, 32, d)$
Conv 3D (Stride 2)	$(4, 4, 4, 2d, 4d)$	$(n, 16, 16, 16, 4d)$
LReLU ($\alpha = 0.2$)		$(n, 16, 16, 16, d)$
Conv 3D (Stride 1)	$(4, 4, 4, d, d)$	$(n, 16, 16, 16, d)$
LReLU ($\alpha = 0.2$)		$(n, 16, 16, 16, d)$
Conv 3D (Stride 2)	$(4, 4, 4, d, d)$	$(n, 8, 8, 8, d)$
LReLU ($\alpha = 0.2$)		$(n, 8, 8, 8, d)$
Reshape		$(n, 512d)$
Dense	$(512d, 1)$	$(n, 1)$

Table 4 Detailed architecture of UpscaleGAN $32^3 \rightarrow 64^3$. $d = 32$.

Author's contributions

NP performed the experiment design and the full analysis. NP and AS contributed to the implementation of the algorithms. Initial implementation of the algorithm was presented in Master's thesis by AS titled "Scalable Generative Models For Cosmology", supervised by NP, AL, and TK, with advice from TH and AR. NP created the challenge. TK and AL initiated the study as the Principle Investigators of the DLOC program at the SDSC, provided the resources used in the analysis, performed the experiment design, and provided direct guidance and supervision. JF and RS prepared the N-body simulations dataset. AR and TH contributed to development of the ideas and the proposal. All authors read and approved the final manuscript.

Acknowledgments

We thank Adam Amara for initial discussions on the project idea. We thank Janis Fluri and Raphael Sgier for help with generating the data. We acknowledge the support of the IT service of the Piz Daint computing cluster at the Swiss National Supercomputing Center (CSCS), as well as the Leonhard and Euler clusters at ETH Zurich.

Author details

¹Swiss Data Science Center, ETH Zurich, Universitätsstrasse 25, 8006 Zurich, Switzerland. ²Institute for Particle Physics and Astrophysics, ETH Zurich, Wolfgang-Pauli-Str. 27, 8093 Zurich, Switzerland. ³Institute for

Machine Learning, ETH Zurich, Universitätstrasse 6, 8006 Zurich, Switzerland.

References

- Goodfellow, I., Pouget-Abadie, J., Mirza, M., Xu, B., Warde-Farley, D., Ozair, S., Courville, A., Bengio, Y.: Generative Adversarial Nets. *Advances in Neural Information Processing Systems*, ??? (2014)
- Karras, T., Aila, T., Laine, S., Lehtinen, J.: Progressive Growing of GANs for Improved Quality, Stability, and Variation. *6th International Conference on Learning Representations (ICLR)*, ??? (2018)
- Springel, V., White, S.D.M., Jenkins, A., Frenk, C.S., Yoshida, N., Gao, L., Navarro, J., Thacker, R., Croton, D., Helly, J., Peacock, J.A., Cole, S., Thomas, P., Couchman, H., Evrard, A., Colberg, J., Pearce, F.: Simulations of the formation, evolution and clustering of galaxies and quasars. *nature* **435**, 629–636 (2005). doi:[10.1038/nature03597](https://doi.org/10.1038/nature03597). [astro-ph/0504097](https://arxiv.org/abs/astro-ph/0504097)
- Potter, D., Stadel, J., Teyssier, R.: PKDGRAV3: Beyond Trillion Particle Cosmological Simulations for the Next Era of Galaxy Surveys. *Computational Astrophysics and Cosmology*, **4**(1):2, ??? (2017)
- Kuhlen, M., Vogelsberger, M., Angulo, R.: Numerical simulations of the dark universe: State of the art and the next decade. *Physics of the Dark Universe* **1**(1-2), 50–93 (2012). doi:[10.1016/j.dark.2012.10.002](https://doi.org/10.1016/j.dark.2012.10.002). [1209.5745](https://arxiv.org/abs/1209.5745)
- Rodríguez, A.C., Kacprzak, T., Lucchi, A., Amara, A., Sgier, R., Fluri, J., Hofmann, T., Réfrégier, A.: Fast cosmic web simulations with generative adversarial networks. *Computational Astrophysics and Cosmology* **5**(1), 4 (2018)
- Mustafa, M., Bard, D., Bhimji, W., Lukić, Z., Al-Rfou, R., Kratochvil, J.M.: CosmoGAN: creating high-fidelity weak lensing convergence maps using Generative Adversarial Networks. *Computational Astrophysics and Cosmology* **6**(1), 1 (2019). doi:[10.1186/s40668-019-0029-9](https://doi.org/10.1186/s40668-019-0029-9). [1706.02390](https://arxiv.org/abs/1706.02390)
- Bond, J.R., Kofman, L., Pogosyan, D.: How Filaments of Galaxies Are Woven Into the Cosmic Web. *Nature*, **380**:603–606, ??? (1996)
- Dietrich, J.P., Werner, N., Clowe, D., Finoguenov, A., Kitching, T., Miller, L., Simionescu, A.: A Filament of Dark Matter Between Two Clusters of Galaxies. *Nature*, **487**:202–204, ??? (2012)
- Zhu, J.-Y., Park, T., Isola, P., Efros, A.A.: Unpaired Image-to-image Translation Using Cycle-consistent Adversarial Networks. *International Conference on Computer Vision (ICCV)*, ??? (2017)
- Satoshi Iizuka, E.S.-S., Ishikawa, H.: Globally and Locally Consistent Image Completion. *ACM Trans. Graph.*, **36**(4):107:1–107:14, ??? (2017)
- Kingma, D.P., Welling, M.: Auto-Encoding Variational Bayes. *Proceedings of the 2nd International Conference on Learning Representations (ICLR)*, ??? (2014)
- van den Oord, A., Kalchbrenner, N., Vinyals, O., Espeholt, L., Graves, A., Kavukcuoglu, K.: Conditional Image Generation with PixelCNN Decoders. *Proceedings of the 30th International Conference on Neural Information Processing Systems*, Pages 4797–4805, ??? (2016)
- Denton, E., Chintala, S., Szlam, A., Fergus, R.: Deep Generative Image Models Using a Laplacian Pyramid of Adversarial Networks. *Advances in Neural Information Processing Systems* **28**, ??? (2015)
- Ledig, C., Theis, L., Huszár, F., Caballero, J., Cunningham, A., Acosta, A., Aitken, A., Tejani, A., Totz, J., Wang, Z., *et al.*: Photo-realistic single image super-resolution using a generative adversarial network. In: *Proceedings of the IEEE Conference on Computer Vision and Pattern Recognition*, pp. 4681–4690 (2017)
- Lai, W.-S., Huang, J.-B., Ahuja, N., Yang, M.-H.: Deep laplacian pyramid networks for fast and accurate super-resolution. In: *Proceedings of the IEEE Conference on Computer Vision and Pattern Recognition*, pp. 624–632 (2017)
- Wang, X., Yu, K., Wu, S., Gu, J., Liu, Y., Dong, C., Qiao, Y., Change Loy, C.: Esgan: Enhanced super-resolution generative adversarial networks. In: *Proceedings of the European Conference on Computer Vision (ECCV)*, pp. 0–0 (2018)
- Brock, A., Donahue, J., Simonyan, K.: Large scale gan training for high fidelity natural image synthesis. *arXiv preprint arXiv:1809.11096* (2018)
- Lucic, M., Tschannen, M., Ritter, M., Zhai, X., Bachem, O., Gelly, S.: High-fidelity image generation with fewer labels. *arXiv preprint arXiv:1903.02271* (2019)
- Chang, C., Pujol, A., Mawdsley, B., Bacon, D., Elvin-Poole, J., Melchior, P., Kovács, A., Jain, B., Leistedt, B., Giannantonio, T.: Dark Energy Survey Year 1 results: curved-sky weak lensing mass map. *MNRAS* **475**(3), 3165–3190 (2018). doi:[10.1093/mnras/stx3363](https://doi.org/10.1093/mnras/stx3363). [1708.01535](https://arxiv.org/abs/1708.01535)
- Schmalzing, J., Kerscher, M., Buchert, T.: Minkowski Functionals in Cosmology. In: Bonometto, S., Primack, J.R., Provenzale, A. (eds.) *Dark Matter in the Universe*, p. 281 (1996). [astro-ph/9508154](https://arxiv.org/abs/astro-ph/9508154)
- He, S., Li, Y., Feng, Y., Ho, S., Ravanbakhsh, S., Chen, W., Póczos, B.: Learning to Predict the Cosmological Structure Formation. *arXiv e-prints*, 1811–06533 (2018). [1811.06533](https://arxiv.org/abs/1811.06533)
- Regier, J., McAuliffe, J., Prabhat: A Deep Generative Model for Astronomical Images of Galaxies. In *NIPS Workshop: Advances in Approximate Bayesian Inference*, ??? (2015)
- Tröster, T., Ferguson, C., Harnois-Déraps, J., McCarthy, I.G.: Painting with baryons: augmenting N-body simulations with gas using deep generative models. *MNRAS* **487**(1), 24–29 (2019). doi:[10.1093/mnras/slz075](https://doi.org/10.1093/mnras/slz075). [1903.12173](https://arxiv.org/abs/1903.12173)
- Schawinski, K., Zhang, C., Zhang, H., Fowler, L., Santhanam, G.K.: Generative Adversarial Networks Recover Features in Astrophysical Images of Galaxies Beyond the Deconvolution Limit. *MNRAS*, **467**:L110–L114, ??? (2017)
- Reiman, D.M., Göhre, B.E.: Deblending galaxy superpositions with branched generative adversarial networks. *MNRAS* **485**(2), 2617–2627 (2019). doi:[10.1093/mnras/stz575](https://doi.org/10.1093/mnras/stz575). [1810.10098](https://arxiv.org/abs/1810.10098)
- Kodi Ramanah, D., Charnock, T., Lavaux, G.: Painting halos from 3D dark matter fields using Wasserstein mapping networks. *arXiv e-prints*, 1903–10524 (2019). [1903.10524](https://arxiv.org/abs/1903.10524)
- Coles, P., Chiang, L.Y.: Characterizing the Nonlinear Growth of Large-scale Structure in the Universe. *Nature*, **406**:376–378, ??? (2000)
- Forero-Romero, J.E., Hoffman, Y., Gottlöber, S., Klypin, A., Yepes, G.: A Dynamical Classification of the Cosmic Web. *MNRAS*, **396**:1815–1824, ??? (2009)
- DES Collaboration: Dark Energy Survey Year 1 Results: Cosmological Constraints from Galaxy Clustering and Weak Lensing. *ArXiv e-prints arxiv.org/abs/1708.01530*, ??? (2017)
- Hildebrandt, H., Viola, M., Heymans, C., Joudaki, S., Kuijken, K., Blake, C., Erben, T., Joachimi, B., Klaes, D., Miller, L., Morrison, C.B., Nakajima, R., Kleijn, G.V., Amon, A., Choi, A., Covone, G., de Jong, J.T.A., Dvornik, A., Conti, I.F., Grado, A., Harnois-Déraps, J., Herbonnet, R., Hoekstra, H., Köhlinger, F., McFarland, J., Mead, A., Merten, J., Napolitano, N., Peacock, J.A., Radovich, M., Schneider, P., Simon, P., Valentijn, E.A., van den Busch, J.L., van Uitert, E., Waerbeke, L.V.: KiDS-450: Cosmological Parameter Constraints from Tomographic Weak Gravitational Lensing. *Monthly Notices of the Royal Astronomical Society*, **465**(2):1454–1498, ??? (2017)
- Joudaki, S., Mead, A., Blake, C., Choi, A., de Jong, J., Erben, T., Conti, I.F., Herbonnet, R., Heymans, C., Hildebrandt, H., Hoekstra, H., Joachimi, B., Klaes, D., Köhlinger, F., Kuijken, K., McFarland, J., Miller, L., Schneider, P., Viola, M.: KiDS-450: Testing Extensions to the Standard Cosmological Model. *MNRAS*, **471**:1259–1279, ??? (2017)
- Springel, V.: The Cosmological Simulation Code GADGET-2. *MNRAS*, **364**:1105–1134, ??? (2005)
- Fosalba, P., Gaztañaga, E., Castander, F.J., Crocce, M.: The MICE Grand Challenge Light-cone Simulation - III. Galaxy Lensing Mocks from All-sky Lensing Maps. *MNRAS*, **447**:1319–1332, ??? (2015)
- Busha, M.T., Wechsler, R.H., Becker, M.R., Erickson, B., Evrard, A.E.: Catalog Production for the DES Blind Cosmology Challenge. In *American Astronomical Society Meeting Abstracts*, volume 221, page 341.07, ??? (2013)
- Teyssier, R., Pires, S., Prunet, S., Aubert, D., Pichon, C., Amara, A., Benabed, K., Colombi, S., Refregier, A., Starck, J.L.: Full-sky Weak-lensing Simulation with 70 Billion Particles. *A&A*, **497**:335–341, ??? (2009)
- Boylan-Kolchin, M., Springel, V., White, S.D.M., Jenkins, A., Lemson, G.: Resolving Cosmic Structure Formation with the Millennium-II Simulation. *MNRAS*, **398**:1150–1164, ??? (2009)
- Schneider, A., Teyssier, R., Potter, D., Stadel, J., Onions, J., Reed, D.S., Smith, R.E., Springel, V., Pearce, F.R., Scoccamarro, R.: Matter

- power spectrum and the challenge of percent accuracy. *J. Cosmology Astropart. Phys.* **2016**(4), 047 (2016). doi:[10.1088/1475-7516/2016/04/047](https://doi.org/10.1088/1475-7516/2016/04/047). [1503.05920](https://arxiv.org/abs/1503.05920)
39. Mead, A.J., Peacock, J.A., Heymans, C., Joudaki, S., Heavens, A.F.: An accurate halo model for fitting non-linear cosmological power spectra and baryonic feedback models. *MNRAS* **454**(2), 1958–1975 (2015). doi:[10.1093/mnras/stv2036](https://doi.org/10.1093/mnras/stv2036). [1505.07833](https://arxiv.org/abs/1505.07833)
 40. Huang, H.-J., Eifler, T., Mandelbaum, R., Dodelson, S.: Modelling baryonic physics in future weak lensing surveys. *MNRAS* **488**(2), 1652–1678 (2019). doi:[10.1093/mnras/stz1714](https://doi.org/10.1093/mnras/stz1714). [1809.01146](https://arxiv.org/abs/1809.01146)
 41. Barreira, A., Nelson, D., Pillepich, A., Springel, V., Schmidt, F., Pakmor, R., Hernquist, L., Vogelsberger, M.: Separate Universe Simulations with IllustrisTNG: baryonic effects on power spectrum responses and higher-order statistics. *MNRAS*, 1784 (2019). doi:[10.1093/mnras/stz1807](https://doi.org/10.1093/mnras/stz1807). [1904.02070](https://arxiv.org/abs/1904.02070)
 42. Howlett, C., Manera, M., Percival, W.J.: L-PICOLA: A Parallel Code for Fast Dark Matter Simulation. *Astronomy and Computing*, 12:109–126, ??? (2015)
 43. Kacprzak, T., Kirk, D., Friedrich, O., Amara, A., Refregier, A., Marian, L., Dietrich, J., Suchyta, E., Aleksić, J., Bacon, D., *et al.*: Cosmology constraints from shear peak statistics in dark energy survey science verification data. *Monthly Notices of the Royal Astronomical Society* **463**(4), 3653–3673 (2016)
 44. Martinet, N., Schneider, P., Hildebrandt, H., Shan, H., Asgari, M., Dietrich, J.P., Harnois-Déraps, J., Erben, T., Grado, A., Heymans, C., *et al.*: Kids-450: cosmological constraints from weak-lensing peak statistics–ii: Inference from shear peaks using n-body simulations. *Monthly Notices of the Royal Astronomical Society* **474**(1), 712–730 (2017)
 45. Heusel, M., Ramsauer, H., Unterthiner, T., Nessler, B., Hochreiter, S.: Gans trained by a two time-scale update rule converge to a local nash equilibrium. In: *Advances in Neural Information Processing Systems*, pp. 6626–6637 (2017)
 46. Fréchet, M.: Sur la distance de deux lois de probabilité. *COMPTES RENDUS HEBDOMADAIRES DES SEANCES DE L ACADEMIE DES SCIENCES* **244**(6), 689–692 (1957)
 47. Vaserstein, L.N.: Markov processes over denumerable products of spaces, describing large systems of automata. *Problemy Peredachi Informatsii* **5**(3), 64–72 (1969)
 48. Dowson, D., Landau, B.: The fréchet distance between multivariate normal distributions. *Journal of multivariate analysis* **12**(3), 450–455 (1982)
 49. Roth, K., Lucchi, A., Nowozin, S., Hofmann, T.: Stabilizing training of generative adversarial networks through regularization. In: *Advances in Neural Information Processing Systems*, pp. 2018–2028 (2017)
 50. Gulrajani, I., Ahmed, F., Arjovsky, M., Dumoulin, V., Courville, A.C.: Improved training of wasserstein gans. In: *Advances in Neural Information Processing Systems*, pp. 5767–5777 (2017)
 51. Arjovsky, M., Chintala, S., Bottou, L.: Wasserstein generative adversarial networks. In: *International Conference on Machine Learning*, pp. 214–223 (2017)
 52. Hinton, G.E.: RMSprop. http://www.cs.toronto.edu/~tijmen/csc321/slides/lecture_slides_lec6.pdf, ??? (2012)
 53. Szegedy, C., Liu, W., Jia, Y., Sermanet, P., Reed, S., Anguelov, D., Erhan, D., Vanhoucke, V., Rabinovich, A.: Going Deeper with Convolutions. *The IEEE Conference on Computer Vision and Pattern Recognition (CVPR)*, 2015, pp. 1–9, ??? (2014)
 54. Vondrick, C., Pirsivash, H., Torralba, A.: Generating videos with scene dynamics. In: *Advances In Neural Information Processing Systems*, pp. 613–621 (2016)
 55. Xiong, W., Luo, W., Ma, L., Liu, W., Luo, J.: Learning to generate time-lapse videos using multi-stage dynamic generative adversarial networks. In: *The IEEE Conference on Computer Vision and Pattern Recognition (CVPR)* (2018)
 56. Saito, M., Matsumoto, E., Saito, S.: Temporal generative adversarial nets with singular value clipping. In: *Proceedings of the IEEE International Conference on Computer Vision*, pp. 2830–2839 (2017)
 57. Mirza, M., Osindero, S.: Conditional Generative Adversarial Nets. *arXiv e-prints*, 1411–1784 (2014). [1411.1784](https://arxiv.org/abs/1411.1784)
 58. Dodelson, S.: *Modern Cosmology*, (2003)
 59. Miyato, T., Kataoka, T., Koyama, M., Yoshida, Y.: Spectral normalization for generative adversarial networks. *arXiv preprint arXiv:1802.05957* (2018)

Operation	Parameter size	Output Shape
Generator		
Input $z \sim \mathcal{N}(0, 1)$	-	$(n, 32, 32, 32, 1)$
Input smooth image	-	$(n, 32, 32, 32, 1)$
Input borders	-	$(n, 32, 32, 32, 7)$
Concatentation	-	$(n, 32, 32, 32, 9)$
InConv 3D (Stride 1)	*	$(n, 32, 32, 32, d)$
LReLU ($\alpha = 0.2$)	-	$(n, 32, 32, 32, d)$
InConv 3D (Stride 1)	*	$(n, 32, 32, 32, d)$
LReLU ($\alpha = 0.2$)	-	$(n, 32, 32, 32, d)$
InConv 3D (Stride 1)	*	$(n, 32, 32, 32, d)$
LReLU ($\alpha = 0.2$)	-	$(n, 32, 32, 32, d)$
InConv 3D (Stride 1)	*	$(n, 32, 32, 32, d)$
LReLU ($\alpha = 0.2$)	-	$(n, 32, 32, 32, d)$
InConv 3D (Stride 1)	*	$(n, 32, 32, 32, d)$
LReLU ($\alpha = 0.2$)	-	$(n, 32, 32, 32, d)$
InConv 3D (Stride 1)	*	$(n, 32, 32, 32, d)$
LReLU ($\alpha = 0.2$)	-	$(n, 32, 32, 32, d)$
InConv 3D (Stride 1)	*	$(n, 32, 32, 32, d)$
LReLU ($\alpha = 0.2$)	-	$(n, 32, 32, 32, d)$
InConv 3D (Stride 1)	*	$(n, 32, 32, 32, 1)$
ReLU	-	$(n, 32, 32, 32, 1)$
Discriminator		
Input generated image	-	$(n, 32, 32, 32, 1)$
Input borders	-	$(n, 32, 32, 32, 7)$
Reshape to a cube	-	$(n, 64, 64, 64, 1)$
Input smooth image	-	$(n, 64, 64, 64, 1)$
Concatentation (+ diff)	-	$(n, 64, 64, 64, 3)$
InConv 3D (Stride 2)	*	$(n, 32, 32, 32, 2d)$
LReLU ($\alpha = 0.2$)	-	$(n, 32, 32, 32, 2d)$
InConv 3D (Stride 1)	*	$(n, 32, 32, 32, 2d)$
LReLU ($\alpha = 0.2$)	-	$(n, 32, 32, 32, 2d)$
InConv 3D (Stride 1)	*	$(n, 32, 32, 32, d)$
LReLU ($\alpha = 0.2$)	-	$(n, 32, 32, 32, d)$
InConv 3D (Stride 1)	*	$(n, 32, 32, 32, d)$
LReLU ($\alpha = 0.2$)	-	$(n, 32, 32, 32, d)$
InConv 3D (Stride 1)	*	$(n, 32, 32, 32, d)$
LReLU ($\alpha = 0.2$)	-	$(n, 32, 32, 32, d)$
InConv 3D (Stride 1)	*	$(n, 32, 32, 32, d)$
LReLU ($\alpha = 0.2$)	-	$(n, 32, 32, 32, d)$
InConv 3D (Stride 2)	*	$(n, 16, 16, 16, d)$
LReLU ($\alpha = 0.2$)	-	$(n, 16, 16, 16, d)$
InConv 3D (Stride 2)	*	$(n, 8, 8, 8, d)$
LReLU ($\alpha = 0.2$)	-	$(n, 8, 8, 8, d)$
Reshape	-	$(n, 16384)$
Compute PSD	-	$(n, 1914)$
Concatenate	-	$(n, 18298)$
Dense	$(18298, 64)$	$(n, 64)$
LReLU ($\alpha = 0.2$)	-	$(n, 64)$
Dense	(6416)	$(n, 16)$
LReLU ($\alpha = 0.2$)	-	$(n, 16)$
Dense	$(16, 1)$	$(n, 1)$

Table 5 Detailed architecture of UpscaleGAN $64^3 \rightarrow 256^3$. $d = 64$. The parameter shape of the inception convolution written InConv is too large to be written in the table.